Electronic Structure of Cubane-Like Vanadium–Nitrogen Cationic Clusters [V$_4$N$_4$]$^+$ and [V$_6$N$_6$]$^+$

Piao He [1], **Jian-Guo Zhang** [2] and **John E. McGrady** [3,*]

[1] College of Chemistry and Chemical Engineering, Central South University, Changsha 410083, China; hepiaodj@163.com

[2] State Key Laboratory of Explosion Science and Technology, Beijing Institute of Technology, Beijing 100081, China; zjgbit@bit.edu.cn

[3] Department of Chemistry, University of Oxford, South Parks Road, Oxford OX1 3QZ, UK

[*] Correspondence: john.mcgrady@chem.ox.ac.uk

check for updates

Abstract: Density Functional Theory and Complete Active Space Self-Consistent Field (CASSCF) methodologies are used to explore the electronic structure of the cationic V–N clusters, [V$_4$N$_4$]$^+$ and [V$_6$N$_6$]$^+$, that have been identified in recent mass spectrometric experiments. Our calculations indicate that both clusters are based on cubane-like fragments of the rock-salt lattice. In the smaller [V$_4$N$_4$]$^+$ cluster, the V–V bonding is delocalized over the tetrahedron, with net bond orders of 1/3 per V–V bond. In [V$_6$N$_6$]$^+$, in contrast, the V–V bonding is strongly localized in the central V$_2$N$_2$ unit, which has a short V=V double bond. CASSCF calculations reveal that both localized and delocalized V–V bonds are highly multi-configurational.

Keywords: clusters; vanadium; density functional theory; CASSCF

1. Introduction

Small clusters of transition metal nitrides, M$_x$N$_y$, represent the simplest models for the active sites in the bulk nitrides that have an important role in heterogeneous catalysis [1–3]. Amongst these, vanadium nitride is a particularly important example, and catalytic applications of both the bulk material and thin films have been reported [4–7]. Metal–metal bonding remains very strong in bulk VN, to the extent that it is an extremely good conductor [8], and the solid also features a high concentration of nitrogen vacancies, giving a range of stoichiometries VN$_x$, where $x \leq 1$ [9,10]. Indeed, low-valent binary compounds of the early transition metal elements are, in general, stabilized by extensive metal–metal bonding; examples include TiN [11] and VO [12], as well as the low-temperature form of VO$_2$ [13]. The nature of the surface sites on non-stoichiometric VN remains a matter of debate, but it is clear that V–V bonding has the potential to drive extensive surface reconstruction that may impact the catalytic performance [1]. In light of this extreme non-stoichiometry in the solid state, small molecular clusters with V:N ratios close to 1 (i.e., V$_x$N$_y$, $x \approx y$) provide an important opportunity to explore the interplay of metal–metal bonding, structure, magnetism and catalytic competence of the vanadium nitride phase. In recent work by Hirabayashi and Ichihashi, particular members of the [V$_x$N$_y$]$^+$ family were shown to be highly active catalysts for ammonia decomposition [14]. Clusters with V:N ratios close to 1.0 were formed by sputtering metal targets with accelerated Xe$^+$ beams in the presence of N$_2$. Prominent peaks in the mass spectrum were assigned to [V$_3$N$_3$]$^+$, [V$_4$N$_4$]$^+$, [V$_5$N$_5$]$^+$ and [V$_6$N$_6$]$^+$, as well as the vanadium-rich species [V$_3$N$_2$]$^+$, [V$_4$N$_3$]$^+$, [V$_5$N$_4$]$^+$ and [V$_6$N$_5$]$^+$. The subsequent reactivity of these ions with NH$_3$ depends critically on their composition, and the equiatomic clusters [V$_4$N$_4$]$^+$ and [V$_6$N$_6$]$^+$ appear to be particularly inert, binding one or two molecules of NH$_3$ without showing any N–H bond cleavage. All other ions, in contrast, lose an equivalent of

H_2 from the bound NH_3 to form $[V_xN_y(NH)]^+$. The relative inertness of $[V_4N_4]^+$ and $[V_6N_6]^+$ led Hirabayashi and Ichihashi to propose structures based on cubane-like architectures, which represent fragments of the rock-salt lattice of the parent nitride—VN. Cubane-like motifs are, in fact, relatively common in gas-phase clusters of binary compounds of the alkali and alkaline earth metals and can be viewed as intermediate stages in the crystal growth process [15–17]. $(NaCl)_x$ clusters, for example, have been shown to adopt rock-salt motifs [18], as have a range of alkaline earth metal-oxide clusters, such as $[M_xO_x]^+$, $[M_{x+1}O_x]^+$ and $[M_xO_x]^{2+}$ (M = Ca, Mg). Amongst the transition metal elements, the nitrides $[Ti_xN_x]^{0/+}$ (x = 4, 6 and 9) show similar structural features [11,19,20].

Our interest in the electronic structure of these cubane clusters lies in the extent to which they are stabilized by metal–metal bonding. Stable, coordinatively saturated cubane clusters are known across much of the transition series (see Figure 1 for selected examples), and many have important roles in biology. Fe_4S_4 clusters, for example, are ubiquitous in biological electron transfer [21] and were amongst the first to be studied using the broken-symmetry approach pioneered by Noodleman [22]. More recently, the remarkable structure of the Fe_7Mo double cubane in the FeMo cofactor in nitrogenase has been revealed [23,24], as has the importance of Mn_3Ca cubane motifs in water oxidation [25]. The presence of multiple bridging ligands between the metals in all these clusters means that whilst metal–metal bonding is possible, it is not absolutely essential for stability, and as a result, the bonding in cubanes spans the entire spectrum from strong covalent to weak exchange coupling. The cyclopentadienyl-capped clusters $Cp_4M_4E_4$ (M = Cr, Mo; E = O, S) [26] are a case in point wherein delocalized covalent bonding in the molybdenum systems gives way to weak exchange coupling in the chromium analogues.

(a) $Cp_4Mo_4S_4$

(b) $Fe_4S_4(SR)_4$
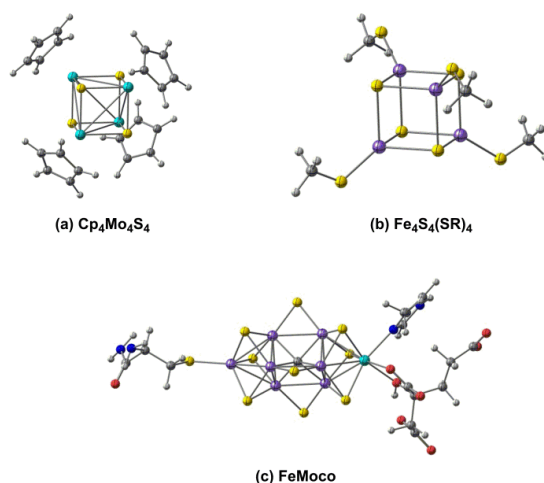
(c) FeMoco

Figure 1. Clusters with cubane-like architectures: (**a**) the $Cp_4M_4E_4$ architecture, (**b**) the Fe_4S_4 cubanes and (**c**) the FeMo cofactor of nitrogenase.

In this paper, we explore the electronic structures of two of the clusters identified in the mass-spectrometric experiments of Hirabayashi and Ichihashi, $[V_4N_4]^+$ and $[V_6N_6]^+$, both of which have been proposed to adopt cubane-like architectures on the basis of their reactivity (or lack thereof) towards ammonia dehydrogenation. The coordinatively unsaturated nature of the metal centres leads to a relatively small splitting within the *d*-orbital manifold, and hence to a very rich electronic structure with many accessible electronic states. From a computational perspective, the description of metal–metal bonding therefore represents a very considerable challenge, and the extent to which single-determinant approaches, such as density functional theory, are appropriate remains to be established. Gorelsky [27] has explored this issue in the context of a vanadium dimer, $V_2(C_5H_5)_2$(pentalene), where both the geometry and the singlet–triplet splitting were found to be well described by the gradient-corrected (GGA) BP86 functional and also by the meta-GGA TPSS functional. The inclusion of exact Hartree–Fock exchange in the B3LYP functional, for example, causes a very substantial weakening of the V–V bond, which appears inconsistent with the available experimental data. In recent work, we identified a

number of other cases where the inclusion of exact exchange in the functional provides a description of metal–metal bonding that is qualitatively different from the picture derived from GGA or meta-GGA functionals [28]. Here, we report results obtained using a range of different density functionals and compare these to the electronic structure picture that emerges from a parallel series of calculations performed with the CASSCF methodology.

2. Results

2.1. Electronic Structure of [V$_4$N$_4$]$^+$

For [V$_4$N$_4$]$^+$, we identified two closely-spaced states, both of which are based on a tetrahedral architecture (Figure 2). The first of these is a ^{4}A$_2$ state with rigorous T_d symmetry: the six V–V bond lengths are identical at 2.65 Å (using the TPSS functional [29]). In the alternative sextet state, ^{6}A$_1$, the tetrahedron is slightly elongated along one of the two-fold axes, giving four long (1.93 Å) and eight short (1.85 Å) V–N bonds and overall D_{2d} symmetry. The average V–V bond lengths in the ^{6}A$_1$ state are somewhat smaller than those in ^{4}A$_2$ (2.60 Å vs. 2.65 Å), while the average V–N bond lengths are marginally longer (1.88 Å vs. 1.86 Å). The origin of these structural patterns is apparent in the Kohn–Sham orbital diagram, also shown in Figure 2. In the perfect tetrahedron, the V d_{z^2} orbitals form a basis for a$_1$ and t$_2$ representations (the z axis is defined locally here as the vector passing through each V atom and the centre of mass of the cluster). The a$_1$ combination is bonding with respect to the V–V interactions but also strongly V–N antibonding, and as a result, it lies above the weakly V–V bonding t$_2$ set. The $d_{xy}/d_{x^2-y^2}$ orbitals, in contrast, are aligned tangentially around the surface of the tetrahedron, and form a basis for e + t$_1$ + t$_2$ representations, the doubly degenerate e orbital being strongly V–V bonding. In the ^{4}A$_2$ state, the two components of the 4e orbital are doubly occupied, while the three components of 12t$_2$ each contain a single electron, giving rise to a perfectly symmetric structure with six equivalent V–V bond lengths of 2.65 Å. Promotion of a single electron from the 4e orbital into 9a$_1$ results in an orbitally degenerate ^{6}E state, and hence to a first-order Jahn–Teller instability that drives the distortion to D_{2d} symmetry (and thus to the ^{6}A$_1$ state). The population of the 9a$_1$ orbital also strengthens the V–V bonds while at the same time weakening the V–N bonds, leading to a global contraction of the V$_4$ tetrahedron.
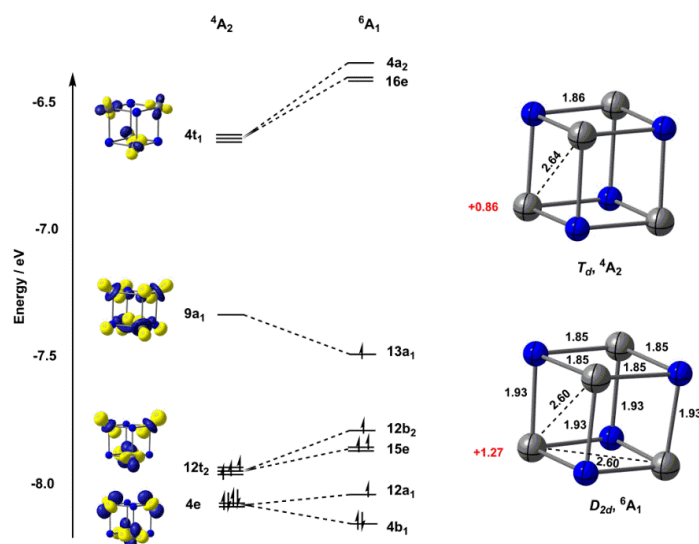
Figure 2. Optimised structures (TPSS/def2-TZVP) and Kohn–Sham molecular orbital diagrams for the quartet (^{4}A$_2$) and sextet (^{6}A$_1$) states of [V$_4$N$_4$]$^+$. Bond lengths (in Å) are shown in black, Mulliken spin densities are shown in red. The levels of the ^{6}A$_1$ state have been shifted upwards by 0.59 eV to bring the barycentre of the 12a$_1$–4b$_1$ pair into coincidence with the 4e level of ^{4}A$_2$.

The structural trends identified in the previous paragraph are broadly independent of the choice of functional (Table 1), but the relative energies of the states are not: with the TPSS functional, the $^6A_1$ state is the global minimum, 0.19 eV lower in energy than $^4A_2$, while with the BP86 functional, the order is reversed, with $^4A_2$ 0.08 eV below $^6A_1$. These behaviours appear to be generally characteristic of the broad classes of functionals (Table 1): the meta-GGAs, TPSS and M06L [30] favour the $^6A_1$ state, while all three GGA functionals (BP86 [31,32], with and without dispersion corrections (Becke–Johnson D3 set [33]), and BLYP [34]) favour $^4A_2$. The hybrid B3LYP functional [35] strongly stabilizes the state of higher multiplicity, a trend that has been observed many times in the literature [36]. Clearly, the balance between one-electron terms, favouring double occupation of the most bonding orbitals, and electron–electron repulsions, favouring higher multiplicities, is a delicate one that challenges even those functionals that have previously proven suitable for metal–metal bonded systems (TPSS and BP86) [27].

Table 1. Relative energies, V–V bond lengths and Mulliken spin densities for the $^4A_2$ and $^6A_1$ states of $[V_4N_4]^+$. The energetic reference point is taken as the more stable of the two states.

Functional	$^4A_2$			$^6A_1$		
	V–V/Å	$\rho(V)$	E_{rel}/eV	V–V/Å	$\rho(V)$	E_{rel}/eV
TPSS	2.64	0.86	+0.19	2.60	1.27	0
M06L	2.62	0.90	+0.38	2.56	1.29	0
BP86	2.65	0.85	0	2.61	1.28	+0.08
BP86-D3	2.65	0.85	0	2.61	1.28	+0.09
BLYP	2.68	0.85	0	2.63	1.28	+0.05
B3LYP	2.62	0.70	+0.65	2.62	1.36	0

In light of the conflicting conclusions about the relative stabilities of $^4A_2$ and $^6A_1$ that emerged from the DFT treatment, we have turned to multi-configurational approaches (specifically the Complete Active Space Self-Consistent Field (CASSCF) methodology) to offer an alternative perspective on the V–V bonding. In both cases, the calculations were performed using the geometry of the corresponding state obtained from the calculations with the TPSS functional, although the precise geometry of a given state is rather independent of the exact choice (with the exception of the M06L functional, which tends to afford rather shorter V–V bonds). The $^4A_2$ and $^6A_1$ states were described using a CAS(7,9) active space, where the nine orbitals include the 4e, $9a_1$ and $12t_2$ orbitals in Figure 2, and also the three additional orbitals of the $4t_1$ set that are derived from the tangential $d_{xy}/d_{x^2-y^2}$ set. The natural orbitals (the orbitals that diagonalise the one-particle density matrix [37,38]) and their occupation numbers are shown in Figure 3 (the orbitals shown are for the $^4A_2$ state, but the iso-surface plots are almost indistinguishable from those for the $^6A_1$ alternative). The three t_2 orbitals had occupations close to 1.0, but the rather low occupations of the 4e orbitals (1.783) and the compensating high values for the $4t_1$ set (0.143) are indicative of strong multi-configurational character. Indeed, the single configuration shown in the Kohn–Sham orbital diagram makes up only 78% of the ground-state wavefunction, the remainder being largely contributions from double excitations from 4e to $4t_1$: these orbitals are bonding–antibonding combinations of the same set of basis functions, and so the strong correlations are consistent with Roos's proposals for an appropriate choice of active space [39,40]. The natural orbital occupations for the $^6A_1$ state (shown in parentheses in Figure 3) confirm a rather similar picture of the bonding: the three components of the $12t_2$ orbital were singly occupied, as were the $9a_1$ orbital and one of the two components of 4e. The one remaining pair in the 4e orbital was strongly correlated with the three members of the $4t_1$ orbital, but their overall occupations were reduced accordingly. In summary, the picture of bonding that emerged from the CASSCF calculations was qualitatively similar to the DFT perspective, with the caveat that the multi-configurational approach highlights the very strong static correlation within the doubly occupied V–V bonding orbitals. At the CASSCF level, the $^4A_2$ state was less stable than the $^6A_1$ alternative by 4.78 eV, but the incorporation of dynamic

correlation using N-electron valence state perturbation (NEVPT2) theory reversed the order, such that the $^4A_2$ state was more stable by 5.88 eV.
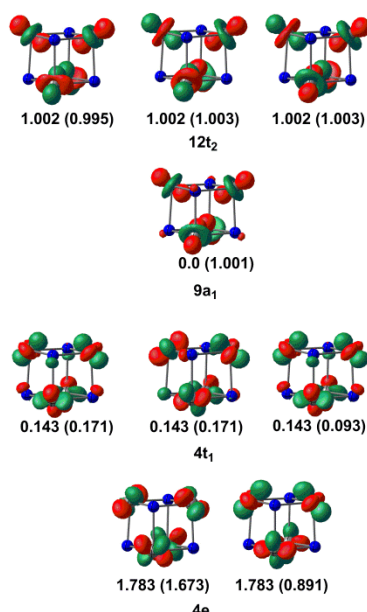
Figure 3. Natural orbital occupations for the $^4A_2$ and $^6A_1$ states (in parentheses) of $[V_4N_4]^+$ with a (7,9) complete active space.

2.2. Electronic Structure of $[V_6N_6]^+$

Turning now to the larger $[V_6N_6]^+$ cluster, we considered a range of structures that have been proposed in the literature for related species, including the columnar fragment of the rock-salt structure proposed by Hirabayashi and Ichihashi (D_{2h} symmetry) and also a hexagonal prismatic structure with two staggered V_3N_3 hexagons (D_{3d} symmetry), which has been identified as the global minimum for the Al_6N_6 cluster [41]. In the case of $[V_6N_6]^+$, this hexagonal structure proved to be over 3 eV higher in energy than the D_{2h} alternative for all functionals, and was not considered further. As was the case for the $[V_4N_4]^+$ cluster, we found a quartet ground state ($^4B_{3g}$) with overall D_{2h} symmetry, with all alternative spin states substantially higher in energy. The V–V bond in the central layer of the cluster (V1–V1) is strikingly short at 2.23 Å (Table 2), a value that is indicative of strong multiple bonding. The bonds between the central and upper/lower layers (V1–V2) were somewhat longer, at 2.52 Å, whilst those within the top and bottom layers (V2–V2) are longer still, at 2.60 Å. All V–V contacts are, however, shorter than those found in either the $^4A_2$ or $^6A_1$ states of $[V_4N_4]^+$. The Kohn–Sham orbitals for the $^4B_{3g}$ state, shown in Figure 4, confirm that, of the eleven available V $3d$ valence electrons, eight are paired in orbitals with significant V–V bonding character. Amongst the doubly occupied set, the $20a_g$ and $15b_{3u}$ orbitals are localized in the central V_2N_2 plane, and have strong V–V σ and V–V π character, respectively, consistent with the presence of a V=V double bond. The $4a_u$ and $10b_{1g}$ orbitals, in contrast, are bonding with respect to all eight V1–V2 contacts between the central plane and the upper/lower layers of the column, accounting for the relatively short distances of 2.51 Å. The remaining three valence electrons occupy the $21a_g$, $14b_{2u}$ and $16b_{3u}$ orbitals, none of which are strongly V–V bonding or antibonding. There are, therefore, many qualitative parallels between the $^4A_2$ state of $[V_4N_4]^+$ and the $^4B_{3g}$ state of $[V_6N_6]^+$: in both cases, some of the available electrons are paired up to form V–V covalent bonds, while the remainder are distributed singly over approximately non-bonding orbitals. The proportion of electrons in the two sets of orbitals changes as a function of the cluster size: for the $^4A_2$ state of $[V_4N_4]^+$, four of the seven available electrons are involved in V–V bonding, while in the $^4B_{3g}$ state of $[V_6N_6]^+$ this fraction rises to 8/11, and the resulting increase in net bond order is behind the generally shorter bond lengths in the larger cluster.

Table 2. V–V bond lengths and Mulliken spin densities for the $^4B_{3g}$ state of $[V_6N_6]^+$.

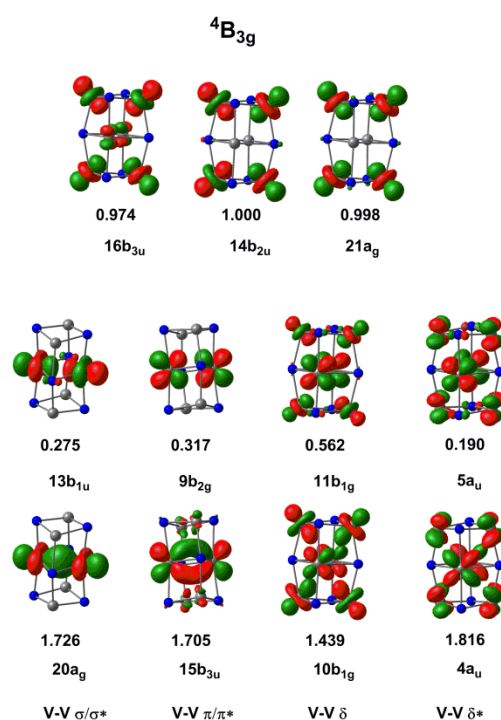| Functional	$^4B_{3g}$	
	V–V/Å [1]	$\rho(V)$ [2]
TPSS	2.23, 2.52, 2.60	−0.10, 0.87
M06L	2.23, 2.51, 2.58	−0.12, 0.92
BP86	2.24, 2.53, 2.62	−0.03, 0.85
BLYP	2.27, 2.55, 2.64	−0.05, 0.86
B3LYP	2.24, 2.53, 2.59	−0.39, 1.07

[1] the three bond lengths correspond to V1–V1, V1–V2 and V2–V2 in Figure 4; [2] spin densities are for V1 and V2.
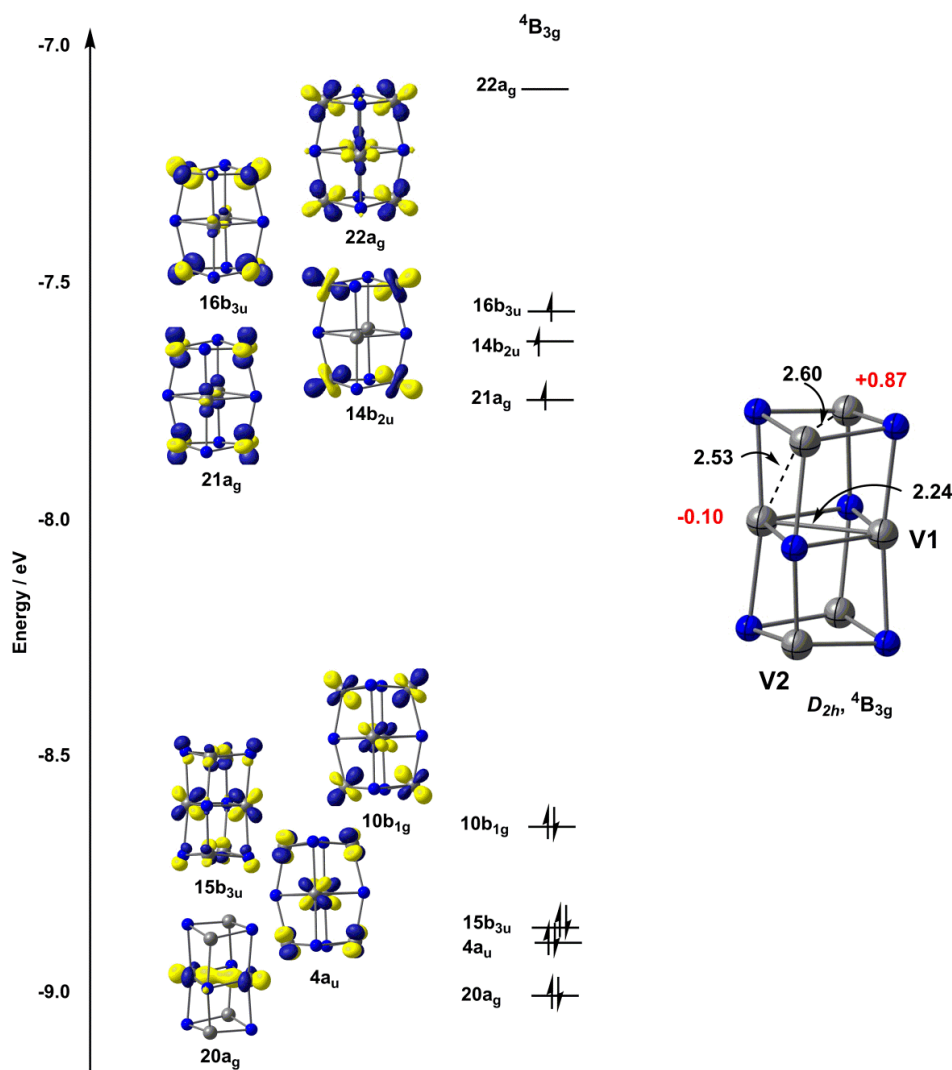
Figure 4. Optimised structure (TPSS/def2-TZVP) and Kohn–Sham molecular orbital diagram for the quartet ($^4B_{3g}$) state of $[V_6N_6]^+$. Bond lengths (in Å) are shown in black, Mulliken spin densities are shown in red.

The CASSCF wavefunction for the $^4B_{3g}$ state of $[V_6N_6]^+$ shown in Figure 5 revealed a qualitatively similar story about the V–V bonding, relative to the one established for $[V_4N_4]^+$. We used a CAS(11,11) active space in which all four doubly occupied bonding orbitals in the Kohn–Sham scheme find antibonding counterparts in the virtual manifold that allow for strong correlations. These are most striking for the V–V σ and π bonds in the central V_2N_2 plane (occupations of the bonding–antibonding pairs are 1.726/0.275 (σ/σ*, $20a_g/13b_{1u}$) and 1.705/0.317 (π/π*, $15b_{3u}/9b_{2g}$)). Natural orbital occupations

that differ dramatically from 2.0 and 0.0 are typical in clusters with multiple metal–metal bonds [42], and are highly indicative of weak bonding. The electrons in the $4a_u$ and $10b_{1g}$ orbitals that mediate the bonding between the layers are also strongly correlated (1.439/0.562 and 1.816/0.190 for the $10b_{1g}/11b_{1g}$ and $4a_u/5a_u$ pairs, respectively). The three remaining singly occupied orbitals are then $21a_g$, $14b_{2u}$ and $16b_{3u}$, all of which have occupations almost equal to 1.0. These three singly occupied orbitals bear a striking resemblance to the three singly occupied components of the t_2 orbital in the $^4A_2$ state of $[V_4N_4]^+$.

$^4\mathbf{B_{3g}}$

| 0.974 | 1.000 | 0.998 |
| $16b_{3u}$ | $14b_{2u}$ | $21a_g$ |

| 0.275 | 0.317 | 0.562 | 0.190 |
| $13b_{1u}$ | $9b_{2g}$ | $11b_{1g}$ | $5a_u$ |

1.726	1.705	1.439	1.816
$20a_g$	$15b_{3u}$	$10b_{1g}$	$4a_u$
V–V $\sigma/\sigma*$	V–V $\pi/\pi*$	V–V δ	V–V $\delta*$

Figure 5. Natural orbital occupations for the $^4B_{3g}$ state of $[V_6N_6]^+$ with a CAS(11,11) active space.

3. Discussion

The two clusters considered here, $[V_4N_4]^+$ and $[V_6N_6]^+$, are both based on fragments of the rock-salt structure, as anticipated by Hirabayashi and Ichihashi in their original report of the mass-spectrometry experiments [14]. In the smaller cluster, quartet and sextet states are very close in energy, and meta-GGA functionals tend to favour the sextet, while GGA functionals predict the quartet to be the ground state. The B3LYP functional, as is typically the case, strongly stabilizes the higher spin state. Our analysis of the Kohn–Sham orbitals indicates that in the $^4A_2$ state, the cluster is stabilized by two pairs of electrons in the V–V bonding 4e orbital, giving a net V–V bond order of 1/3 and a perfectly tetrahedral geometry. The sextet ($^6A_1$), in contrast, is D_{2d}-symmetric, with the distortion away from a perfect tetrahedron being driven by a first-order Jahn–Teller instability. The V–V bonds are shorter and stronger in the $^6A_1$ state as a result of the single occupation of the V–V bonding $9a_1$ orbital, but this is compensated for by a weakening of the V–N bonds. CASSCF calculations (CAS(9,7) active space) are consistent with the picture of bonding that emerges from the DFT calculations, but also reveal the strongly multi-configurational nature of the V–V bonding, which leads to low (<<2.0) occupancies of the 4e orbitals with compensating populations in the V–V antibonding $4t_1$ set. The ground state of the larger $[V_6N_6]^+$ cluster appears to be less controversial: a $^4B_{3g}$ state is the most stable for all functionals considered here, and also at the NEVPT2 level. The cluster is stabilized by a strong V=V double bond between the metal atoms in the central V_2N_2 layer, a feature that emerges irrespective of the chosen theoretical model. In the DFT calculations, the $20a_g$ (V–V σ) and $15b_{3u}$ (V–V π) orbitals are doubly occupied, and the three unpaired electrons in the $^4B_{3g}$ ground state are localized on the upper and

lower layers. To a first approximation, the cluster can therefore be viewed as a diamagnetic central V_2N_2 unit, with radical character delocalized over the upper and lower planes. CASSCF calculations support this basic model, but the multi-configurational character of the V=V double bond is again prominent, with occupations of the σ and π bonding and antibonding orbitals around 1.70 and 0.30. The balance between localized multiple V–V bonding in $[V_6N_6]^+$ and the more delocalized situation in $[V_4N_4]^+$ hints at a subtle relationship between structural and electronic properties, which may have important consequences for the reactivity of the nitrogen-deficient clusters, $[V_{n+1}N_n]^+$. These will be the subject of subsequent studies.

4. Computational Methods

All DFT calculations reported in this paper were performed using Gaussian 16, revision A.03 [43] while the CASSCF calculations were done with ORCA, version 4.0 [44]. Density functional calculations were performed using Ahlrichs's def2-TZVP basis set [45] on V and N either using the meta-GGA TPSS or M06L functionals, the GGA alternatives, BLYP or BP86, or the hybrid B3LYP. CASSCF calculations were performed using the same TZVP basis set and the RIJCOSX approximation to the exchange terms [46]. Dynamic correlation was accounted for using the N-electron valence state perturbation theory (NEVPT2) [47]. All optimised energies and geometries are summarised in Table S1, Supplementary Materials.

5. Conclusions

In this paper we used a combination of density functional theory and correlated ab initio theory (CASSCF) to explore the nature of the bonding in two clusters, $[V_4N_4]^+$ and $[V_6N_6]^+$, which have been observed in mass-spectrometry experiments. Unlike clusters with similar composition, both $[V_4N_4]^+$ and $[V_6N_6]^+$ are remarkably resistant to further reaction with NH_3, suggesting that they share some unique structural and/or electronic features. Our calculations confirm that the two clusters are based on cubic architectures and can be viewed, to a first approximation, as fragments of the rock-salt lattice. However, it is clear that direct covalent V–V bonding plays a very substantial part in stabilizing these structures, just as it does in the low-valent solid phases with similar compositions, such as VN and VO. This bonding is particularly well-developed in the quartet ground state of the $[V_6N_6]^+$ cluster, where a localized V=V double bond is present in the waist of the cluster. The DFT and CASSCF approaches offer broadly equivalent pictures of the metal–metal bonding, but the multi-configurational approach highlights the very strong static correlation that is typical of metal–metal bonds, particularly amongst the first transition series. The strong V–V bonds, along with the very symmetric structure, are consistent with the observed resistance of these two clusters to further reactions. Future work will focus on the interplay between V–V bonding and catalytic activity for the less symmetric nitrogen-deficient clusters, $[V_4N_3]^+$ and $[V_6N_5]^+$, both of which are substantially more reactive [14].

Author Contributions: Investigation, J.E.M. and P.H.; Project administration, J.E.M.; Supervision, J.E.M. and J.-G.Z.; Writing—original draft, P.H.; Writing—review & editing, J.E.M.

References

1. Hargreaves, J.S.J. Heterogeneous catalysis with metal nitrides. *Coord. Chem. Rev.* **2013**, *257*, 2015–2031. [CrossRef]
2. Guo, J.; Wang, P.; Wu, G.; Wu, A.; Hu, D.; Xiong, Z.; Wang, J.; Yu, P.; Chang, F.; Chen, Z.; et al. Lithium imide synergy with 3d transition-metal nitrides leading to unprecedented catalytic activities for ammonia decomposition. *Angew. Chem. Int. Ed.* **2015**, *54*, 2950–2954. [CrossRef]

3. Lotz, C.R.; Sebba, F. Energies of activation for decomposition of ammonia catalysed by the nitrides of the 4th series transition elements. *Trans. Faraday Soc.* **1957**, *53*, 1246–1252. [CrossRef]

4. Liao, M.Y.; Gotoh, Y.; Tsuji, H.; Ishikawa, J. Crystallographic structure and composition of vanadium nitride films deposited by direct sputtering of a compound target. *J. Vac. Sci. Technol. A* **2004**, *22*, 146–150. [CrossRef]

5. Abghoui, Y.; Garden, A.L.; Howalt, J.G.; Vegge, T.; Skúlason, E. Electroreduction of N_2 to ammonia at ambient conditions on mononitrides of Zr, Nb, Cr, and V: A DFT guide for experiments. *ACS Catal.* **2016**, *6*, 635–646. [CrossRef]

6. Choi, D.; Blomgren, G.E.; Kumta, P.N. Fast and reversible surface redox reaction in nanocrystalline vanadium vitride supercapacitors. *Adv. Mater.* **2006**, *18*, 1178–1182. [CrossRef]

7. McGill, W.J.; Sebba, F. The kinetics of ammonia decomposition over vanadium nitride. *J. Catal.* **1963**, *2*, 104–108. [CrossRef]

8. Zhou, X.; Shang, C.; Gu, L.; Dong, S.; Chen, X.; Han, P.; Li, L.; Yao, J.; Liu, Z.; Xu, H.; et al. Mesoporous coaxial titanium nitride–vanadium nitride fibers of core–shell structures for high-performance supercapacitors. *ACS Appl. Mater. Interfaces* **2011**, *3*, 3058–3063. [CrossRef] [PubMed]

9. Indlekofer, G.; Mariot, J.M.; Lengauer, W.; Beauprez, E.; Oelhafen, P.; Hague, C.F. Electronic structure of stoichiometric and substoichiometric vanadium nitrade from photoelectron spectroscopy. *Solid State Commun.* **1989**, *72*, 419–423. [CrossRef]

10. Wu, G.; Yang, M.; Guo, X.; Wang, J. Comparative DFT study of N_2 and NO adsorption on vanadium clusters V_n (n = 2–13). *J. Comput. Chem.* **2012**, *33*, 1854–1861. [CrossRef] [PubMed]

11. Reddy, B.V.; Khanna, S.N. Structure and stability of Ti_nN_m clusters. *Phys. Rev. B* **1996**, *54*, 2240–2243. [CrossRef]

12. Jakubikova, E.; Rappé, A.K.; Bernstein, E.R. Density functional theory study of small vanadium oxide clusters. *J. Phys. Chem. A* **2007**, *111*, 12938–12943. [CrossRef]

13. Aetukuri, N.B.; Gray, A.X.; Drouard, M.; Cossale, M.; Gao, L.; Reid, A.H.; Kukreja, R.; Ohldag, H.; Jenkins, C.A.; Arenholz, E.; et al. Control of the metal–insulator transition in vanadium dioxide by modifying orbital occupancy. *Nat. Phys.* **2013**, *9*, 661–666. [CrossRef]

14. Hirabayashi, S.; Ichihashi, M. Adsorption and dehydrogenation of ammonia on vanadium and niobium nitride cluster cations. *Int. J. Mass Spectrom.* **2016**, *407*, 86–91. [CrossRef]

15. Pralong, V. Lithium intercalation into transition metal oxides: A route to generate new ordered rock salt type structure. *Prog. Solid State Chem.* **2009**, *37*, 262–277. [CrossRef]

16. Burdett, J.K.; Mitchell, J.F. Nonstoichiometry in early transition metal compounds with the rock salt structure. *Prog. Solid State Chem.* **1995**, *23*, 131–170. [CrossRef]

17. Liu, Q.Q.; Pan, H.L.; Tao, W.H.; Wu, H.T. New rock salt structure dielectric material $Li_2Ni_3TiO_6$ at microwave frequency. *J. Mater. Sci: Mater. Electron.* **2017**, *28*, 9893–9899. [CrossRef]

18. Nakamura, A.; Ukita, M.; Shimoda, N.; Furushima, Y.; Toyoura, K.; Matsunaga, K. First-principles calculations on slip system activation in the rock salt structure: Electronic origin of ductility in silver chloride. *Philos. Mag.* **2017**, *97*, 1281–1310. [CrossRef]

19. Chen, Z.Y.; Castleman, A.W., Jr. Growth of titanium nitride: From clusters to microcrystals. *J. Chem. Phys.* **1993**, *98*, 231–235. [CrossRef]

20. Marksteiner, P.; Weinberger, P.; Neckel, A.; Zeller, R.; Dederichs, P.H. Electronic structure of substoichiometric carbides and nitrides of titanium and vanadium. *Phys. Rev. B* **1986**, *33*, 812–822. [CrossRef]

21. Beinert, H.; Holm, R.H.; Münck, E. Iron–sulfur clusters: Nature's modular, multipurpose structures. *Science* **1997**, *277*, 653–659. [CrossRef] [PubMed]

22. Noodleman, L. A model for the spin states of high-potential iron–sulfur $[Fe_4S_4]^{3+}$ proteins. *Inorg. Chem.* **1988**, *27*, 3677–3679. [CrossRef]

23. Lancaster, K.M.; Roemelt, M.; Ettenhuber, P.; Hu, Y.; Ribbe, M.W.; Neese, F.; Bergmann, U.; DeBeer, S. X-ray emission spectroscopy evidences a central carbon in the nitrogenase iron-molybdenum cofactor. *Science* **2011**, *334*, 974–977. [CrossRef] [PubMed]

24. Bjornsson, R.; Neese, F.; DeBeer, S. Revisiting the Mössbauer isomer shifts of the FeMoco cluster of nitrogenase and the cofactor charge. *Inorg. Chem.* **2017**, *56*, 1470–1477. [CrossRef]

25. Krewald, V.; Neese, F.; Pantazis, D.A. On the magnetic and spectroscopic properties of high-valent Mn_3CaO_4 cubanes as structural units of natural and artificial water-oxidizing catalysts. *J. Am. Chem. Soc.* **2013**, *135*, 5726–5739. [CrossRef] [PubMed]

26. McGrady, J.E. Periodic trends in metal–metal bonding in cubane clusters, $(C_5H_5)_4M_4E_4$ [M = Cr, Mo, E = O, S]. *J. Chem. Soc. Dalton Trans.* **1999**, 1393–1400. [CrossRef]

27. Gorelsky, S.I. Complexes with a single metal–metal bond as a sensitive probe of quality of exchange-correlation functionals. *J. Chem. Theor. Comput.* **2012**, *8*, 908–914. [CrossRef]

28. Spivak, M.; Arcisauskaite, V.; López, X.; McGrady, J.E.; de Graaf, C. A multiconfigurational approach to the electronic structure of trichromium extended metal atom chains. *Dalton Trans.* **2017**, *46*, 6202–6211. [CrossRef] [PubMed]

29. Tao, J.M.; Perdew, J.P.; Staroverov, V.N.; Scuseria, G.E. Climbing the density functional ladder: Nonempirical meta-generalized gradient approximation designed for molecules and solids. *Phys. Rev. Lett.* **2003**, *91*, 146401:1–146401:4. [CrossRef] [PubMed]

30. Zhao, Y.; Truhlar, D.G. A new local density functional for main-group thermochemistry, transition metal bonding, thermochemical kinetics, and noncovalent interactions. *J. Chem. Phys.* **2006**, *125*, 194101:1–194101:18. [CrossRef]

31. Becke, A.D. Density-functional exchange-energy approximation with correct asymptotic behavior. *Phys. Rev. A* **1988**, *38*, 3098–3100. [CrossRef]

32. Perdew, J.P. Density-functional approximation for the correlation energy of the inhomogeneous electron gas. *Phys. Rev. B* **1986**, *33*, 8822–8824. [CrossRef]

33. Stefan, G.; Stephan, E.; Lars, G. Effect of the damping function in dispersion corrected density functional theory. *J. Comp. Chem.* **2011**, *32*, 1456–1465.

34. Lee, C.; Yang, W.; Parr, R.G. Development of the Colle-Salvetti correlation-energy formula into a functional of the electron density. *Phys. Rev. B* **1988**, *37*, 785–789. [CrossRef]

35. Becke, A.D. Density-functional thermochemistry. III. The role of exact exchange. *J. Chem. Phys.* **1993**, *98*, 5648–5652. [CrossRef]

36. Paulsen, H.; Trautwein, A.X. Density functional theory calculations for spin-crossover complexes. *Top. Curr. Chem.* **2012**, *235*, 197–219.

37. Davidson, E.R. Natural orbitals. *Adv. Quant. Chem.* **1972**, *6*, 235–266.

38. Davidson, E.R. Properties and uses of natural orbitals. *Rev. Mod. Phys.* **1972**, *44*, 451–464. [CrossRef]

39. Roos, B.O. The complete active space self-consistent field method and its applications in electronic structure calculations. *Adv. Chem. Phys.* **1987**, *69*, 399–445.

40. Veryazov, V.; Malmqvist, P.A.; Roos, B.O. How to select active space for multiconfigurational quantum chemistry? *Int. J. Quantum Chem.* **2011**, *111*, 3329–3338. [CrossRef]

41. Kandalam, A.K.; Blanco, M.A.; Pandey, R. Theoretical study of Al_nN_n, Ga_nN_n, and In_nN_n ($n = 4, 5, 6$) clusters. *J. Phys. Chem. B* **2002**, *106*, 1945–1953. [CrossRef]

42. Li, M.G.; Dzubak, A.L.; Mulla, A.; Brogden, D.W.; Berry, J.F.; Gagliardi, L. Assessing metal–metal multiple bonds in Cr–Cr, Mo–Mo, and W–W compounds and a hypothetical U–U compound: A quantum chemical study comparing DFT and multireference methods. *Chem. Eur. J.* **2012**, *18*, 1737–1749.

43. Frisch, M.J.; Trucks, G.W.; Schlegel, H.B.; Scuseria, G.E.; Robb, M.A.; Cheeseman, J.R.; Scalmani, G.; Barone, V.; Petersson, G.A.; Nakatsuji, H.; et al. *Gaussian 16, Revision A.03*; Gaussian, Inc.: Wallingford, CT, USA, 2016.

44. Neese, F. Software update: The ORCA program system, version 4.0. *WIREs Comput. Mol. Sci.* **2018**, *8*. [CrossRef]

45. Schäfer, A.; Huber, C.; Ahlrichs, R. Fully optimized contracted Gaussian basis sets of triple zeta valence quality for atoms Li to Kr. *J. Chem. Phys.* **1994**, *100*, 5829–5835. [CrossRef]

46. Neese, F. An improvement of the resolution of the identity approximation for the formation of the Coulomb matrix. *J. Comp. Chem.* **2003**, *24*, 1740–1747. [CrossRef]

47. Angeli, C.; Cimiraglia, R.; Evangelisti, S.; Leininger, T.; Malrieu, J.-P. Introduction of N-electron valence states for multireference perturbation theory. *J. Chem. Phys.* **2001**, *114*, 10252–10264. [CrossRef]